Electronic Supplementary Material (ESI) for Energy & Environmental Science.
This journal is © The Royal Society of Chemistry 2023

Supporting Information

Broadening solid ionic conductor selection for sustainable and earth-abundant solid-state lithium metal batteries

*Peichao Zou,[#] Chunyang Wang,[#] Yubin He, Huolin L. Xin**

P. Z., C. W., Y. H., H. L. X.

Department of Physics and Astronomy, University of California, Irvine, California 92697, United States

[#]These authors contributed equally to this work.

*Corresponding author. E-mail: huolinx@uci.edu

Experimental Section/Methods

*Preparation of UVEA film***.** The UVEA film was synthesized by a single-step, solvent-free UV polymerization approach. A liquid precursor was firstly prepared by mixing the monomer (ethylene acrylate, EA, Sigma Aldrich, 9.52 wt.%), cross-linker (ethylene glycol dimethyl acrylate, EDA, Sigma Aldrich, , 9.52 wt.%), lithium salt (lithium bis (trifluoromethanesulfonyl) imide, LiTFSI, Sigma Aldrich, 28.57 wt.%), solid crystal plasticizer (succinonitrile, SN, TCI,), photo-initiator (phenylbis (2,4,6-trimethylbenzoyl) phosphineoxide, PPO, 0.5 wt.%, TCI, 47.62 wt.%), and SEI-forming additive (fluoroethylene carbonate, FEC, TCI, 4.77 wt.%). The obtained homogenous precursor was then casted onto a 340 μm-thick glass fiber reinforcement, and then exposed to UV irradiation for 10 minutes to initiate the polymerization. The obtained UVEA film was then stored inside glove box before use.

*Fabrication of inorganic LICs pellets***.** The inorganic LATP layer was produced by pressing the commercial fine LATP powders (from NEI corporation) into round pellets using a cylindrical die (diameter = 13 mm) followed by annealing at 1150 ^{o}C for 12 h at air. The as-fabricated LATP pellets after annealing have a thickness of around 0.5 mm. The inorganic LVO layer was fabricated using the similar pressing method yet without annealing, in which the pristine LVO powders were synthesized through a sol-gel method adapted from previous reports.[1, 2] Robust LVO pellets with grainy and smooth surface can be directly obtained via the cold-pressing protocol, largely owing to the small particle size (Figure S16b, c). Similarly, LTO pellets (the powder is from MTI Corporation USA) and NMC811 pellets (the powder is from the Cell Analysis, Modeling, and Prototyping (CAMP) facility at Argonne National Lab) were fabricated using the cold pressing method. The thickness of all inorganic LIC pellets was controlled at about 400 um, unless stated otherwise.

*Preparation of sandwich SSE and composite SSE***.** After obtaining the free-standing UVEA films and inorganic LIC ceramic pellets, the sandwich SSEs (in a configuration of UVEA-inorganic LIC-UVEA) were achieved by physically stacking the UVEA film, one inorganic LIC layer, and the UVEA film together. The composite SSEs (in a configuration of UVEA+inorganic LIC) was prepared by uniformly mixing inorganic LIC powder with the UVEA precursor, then casting the

slurry onto a 340 μm-thick glass fiber reinforcement, and finally exposing to the UV irradiation for 10 minutes. The mass ratio of inorganic LIC powder over the UVEA precursor was 1 : 10.

*In-situ coating of UVEA film on inorganic LICs pellets***.** To lower the thickness of solid separator (UVEA), in-situ coating of UVEA film on inorganic LIC pellets was used. Specifically, UVEA precursor (before polymerization) was first dip-coated or spin-coated on the ceramic pellets in an Ar-filled glove box, following by the UV irradiation for 10 minutes. During the spin-coating process, the spinning speed was 2000 r/min and the spinning time was 30s.

*Materials characterization***.** SEM images were obtained with a LEXI-FEI Magellan 400. X-ray photoelectron spectroscopy (XPS) data was collected on a Kratos AXIS-Supra connected with an Ar glove box. The Cryo-TEM imaging and chemical analysis were performed with a Cryo-TEM holder (Gatan model 915) in a JOEL Grand ARM electron microscope (equipped with dual 100 mm^2 silicon drift detectors (SDD) for EDS) operated at 300 kV and a 2100F electron microscope operated at 200 kV. To prepare the Cryo-TEM sample, a 2032-type coin cell was assembled by inserting a copper grid (3mm in diameter) onto the Cu electrode (a Li metal foil works as the counter electrode) in an argon-protected glovebox. After depositing 0.5 mAh cm^{-2} of Li^0 on a Cu grid at a current density of 0.1 mA cm^{-2}, the coin cell was disassembled, and the copper grid was sealed inside a pouch bag in an argon-protected glovebox. The copper grid was plunged into a bath pre-cooled with liquid nitrogen, and finally, the TEM sample was fixed onto the Cryo-TEM holder and transferred into the microscope at the cryogenic temperature for further characterizations. Dynamic mechanical analysis (DMA) was used to analyze the mechanical properties of UVEA film. The liquid-state ^1H NMR measurement was first conducted to determine the monomer conversion yield in UVEA film after polymerization. During the test, the prepared UVEA films were soaked in dimethyl sulfoxide (DMSO) for 10 h and the obtained solution was used to the NMR characterization. The TGA-DSC-MS measurement was conducted using the NETZSCH STA 449 F3 Jupiter Simultaneous Thermal Analyzer with Coupled QMS 403 D Aëolos Mass Spectrometer.

*Electrochemical performance evaluation***.** The electrochemical performance of sandwich SSEs was evaluated using the standard 2032-type coin cells, which was assembled with a constant pressure of 20 MPa in a glove box. Electrochemical impedance spectroscopy (EIS) was recorded

on a Bio-logic working station at the frequency range of 3 MHz to 1 Hz. Ionic conductivities were measured by sandwiching bare UVEA film or inorganic LICs pellets between two stainless steel spacers, and then calculated according to the following equation:

$$\sigma = L/R_bS \qquad \text{Equation (1)}$$

where R_b refers to the resistance according to the EIS measurement, L represents the thickness of testing samples, and S is the effective contacting area between stainless steel spacers and samples.

The electronic conductivity of bare UVEA film and inorganic LIC pellets was obtained by collecting the current response under a constant voltage (0.15V for UVEA film and 3 V for inorganic LIC pellets). During the measurement, the bare UVEA film was directly sandwiched between two stainless steel spacers (blocking electrode), while inorganic LIC pellets were first coated with a thin conductive Ag paste (cured at 250 ^{o}C for 10 min) and then sandwiched between two stainless steel spacers. The electronic conductivity of different LIC pellets/films was calculated as follows:

$$\sigma = L/RS = IL/US \qquad \text{Equation (2)}$$

where I is the average current response, L is the thickness of testing samples, U is the applied voltage (3 V or 0.15 V), and S is the contact area between stainless steel and samples.

The electrochemical stability window (ESW) of UVEA film was tested in a two-electrode Li//UVEA//SS cell, where Li foil was used as the counter electrode, SS (stainless steel) was used as the working electrode, and UVEA was employed as the solid separator. During the test, the Li//UVEA//SS cell was first scanned from open-circuit voltage (OCV) down to -0.3V, and then up to 4.6 V (vs. Li^+/Li). The scanning rate was 0.1 mV/s.

For the Li//NMC811 full cell test, high mass-loading (7.4 mg cm^{-2}) NMC811 cathodes (A-C019A) were directly obtained from the CAMP facility at Argonne National Lab and vacuum dried at 60 ^{o}C before use, where the cathode was composed of Targray NMC811 (90 wt.%), Timcal C-45 (5 wt.%), and Solvay 5130 PVDF binder (5 wt.%). Li-excess Li//NMC811 full cells were assembled in the glove box by using commercial 250 μm-thick Li^0 foils as the anode, as-fabricated sandwich SSEs, and a dried NMC811 cathode (without soaking catholyte), and then cycled at room temperature (22^{o}C) with a NEWARE multichannel cycler. For the construction of low-N/P-ratio full cells, electrodeposited Li^0 on Cu foil with an areal capacity of 2 mAh cm^{-2} was used as the anode. Note that no catholyte was used in all full cells. The Li metal electrodeposition on Cu foil was realized in an asymmetric Li//Cu cell configuration using our recently developed ether-based

localized high-concentration electrolyte with trimethylsilyl azide as the additive.[3] The Li//Cu cell was firstly activated for 1 cycle at 0.5 mA cm^{-2} (with a cycling capacity of 1 mAh cm^{-2}), followed by plating 2 mAh cm^{-2} of Li metal at 0.5 mA cm^{-2}. The typical voltage-time profile is shown in Figure S27. Based on the areal capacity of NMC811, 1.6 mAh cm^{-2} (with a reversible capacity of 210 mAh g^{-1}), the N/P ratio of Li//NMC811 full cells was calculated to be 2.25 when using 2 mAh cm^{-2} of electrodeposited Li^0 as the anode. 1C rate corresponds to a current density of 210 mA g^{-1} for the NMC811 cathode test, meaning that the theoretical capacity of NMC811 cathodes was considered to be 210 mAh g^{-1}.

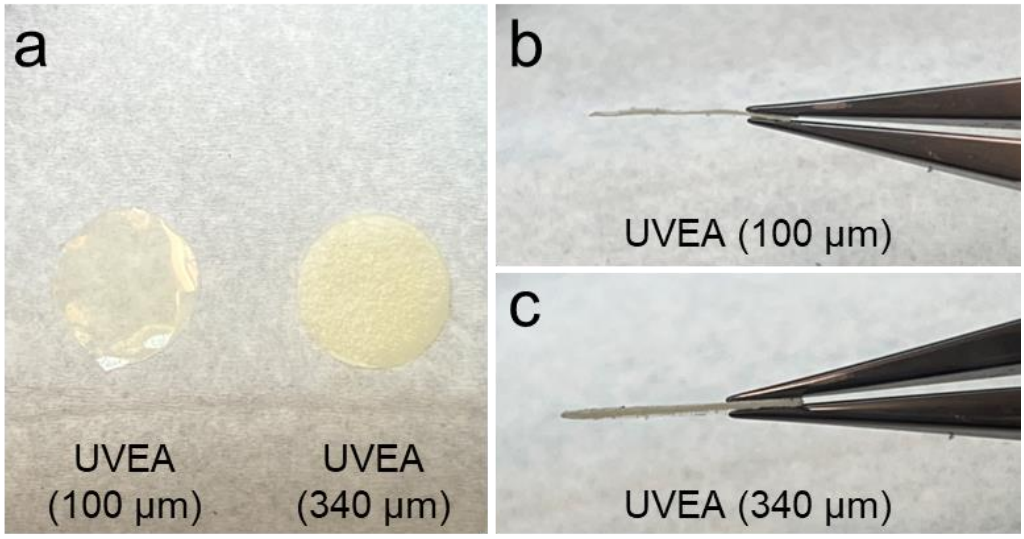

Figure S1. Digital images of UVEA films with two different thicknesses of 340 μm and 100 μm, where glass fiber membrane and PVDF membrane were used as the support substrate, respectively.

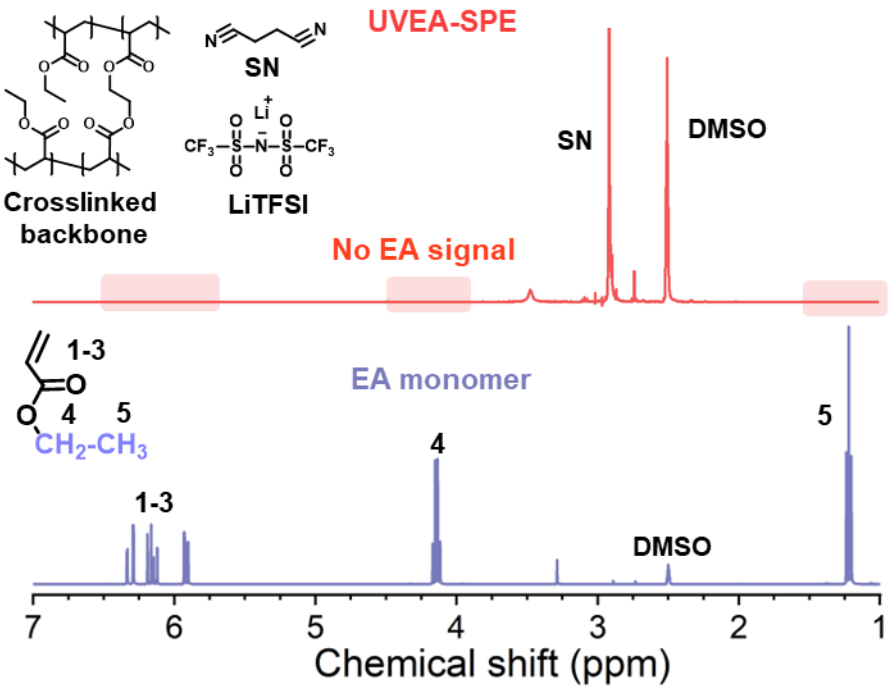

Figure S2. ^{1}H NMR spectra of polymerized UVEA film (up) and ethylene acrylate (EA) monomer (bottom).

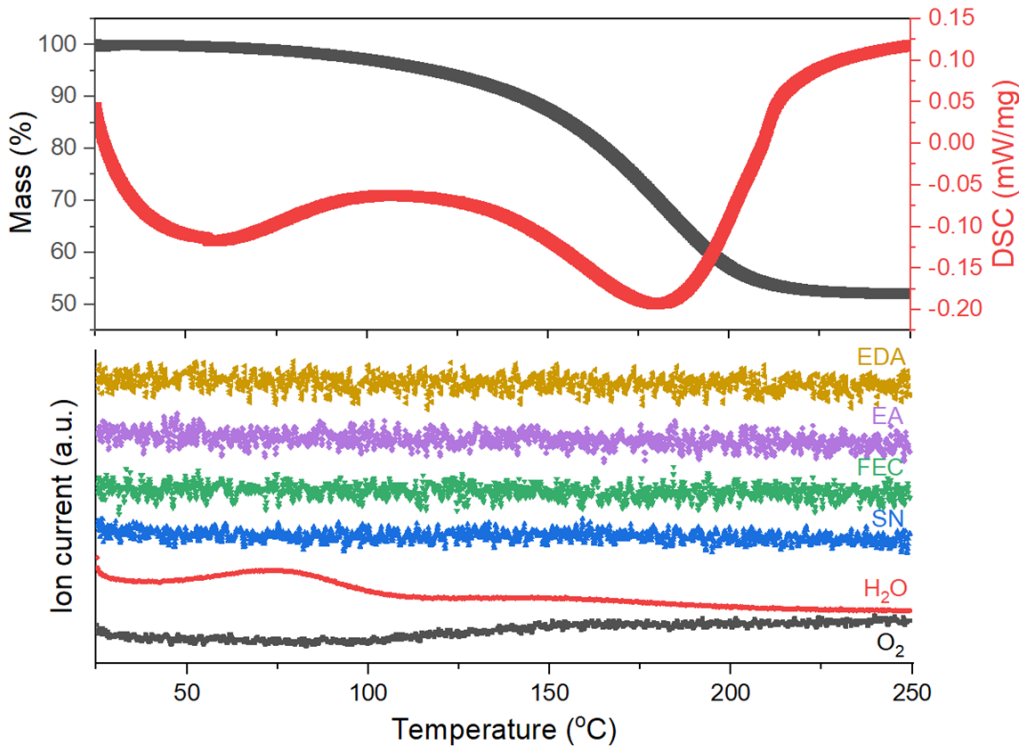

Figure S3. TGA-DSC-MS data showing the weight change and gaseous product release upon heating from 25 °C to 250 °C at a heating rate of 3 °C/min in Ar atmosphere.

Here, the TGA-DSC-MS test indicates that there is no gaseous monomer, cross-linker, plasticizer, and additive release before 250 °C. Knowing that the boiling point of neat EA (99.4 °C), EDA (around 100 °C), and FEC (212 °C) is lower than 250 °C, it is reasonable to deduce that EA and EDA have been completely polymerized in UVEA, and there is no free FEC additive in UVEA. The H_2O signal before 100 °C is derived from the absorbed H_2O on UVEA when loading samples into the test chamber. The O_2 release along with about 45 % weight loss after 110 °C and before 220 °C is probably attributed to the thermal decomposition of the polymer backbone, because the thermal decomposition temperature of LiTFSI, SN plasticizer, and FEC additive is above 200 °C.[4, 5] Since the plasticizer (succinonitrile) is solid at room temperature and has a high boiling point of 266 °C, we can conclude that UVEA film was 100%-monomer-polymerized and can be considered solid at room temperature.

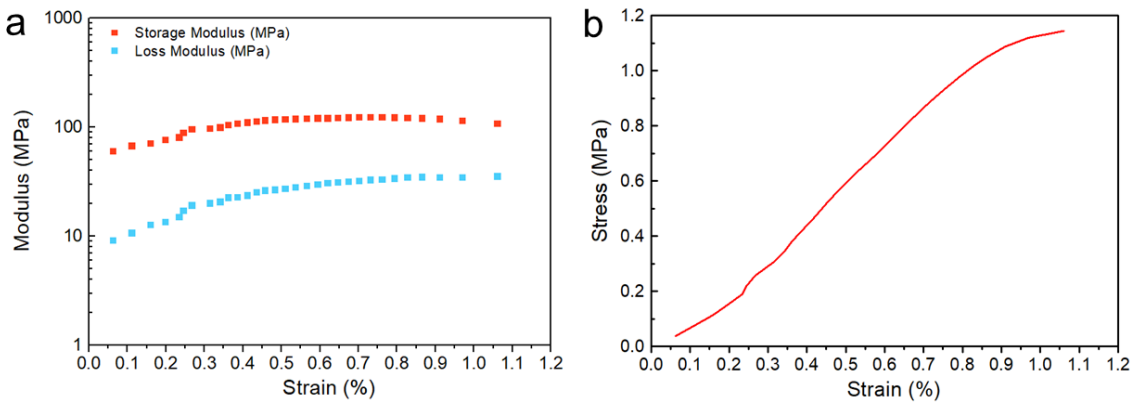

Figure S4. (a) Storage modulus and loss modulus and (b) Stress-strain curve of UVEA measured by dynamic mechanical analysis.

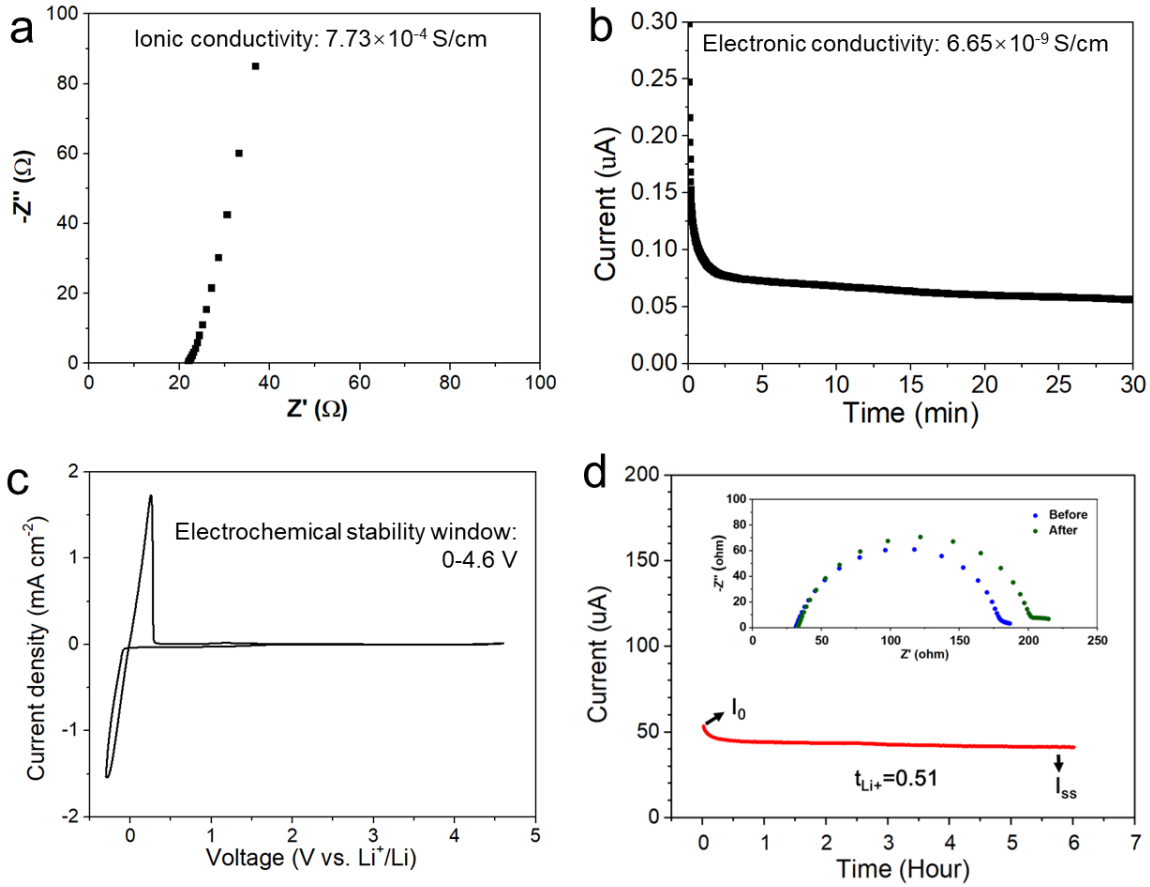

Figure S5. (a) EIS curve of SS//UVEA//SS cell (SS represents the stainless steel) during the ionic conductivity test, in which the thickness and surface area of UVEA film is 340 μm and 2 cm^2, respectively. (b) Electronic conductivity test of pristine UVEA film with a thickness of 340 μm. The applied voltage during the test was controlled at 0.15 V. (c) Electrochemical stability window test of UVEA film in the Li//SS cell, which was conducted at a scan rate of 0.1 mV/s. (d) Li^+ transference number of UVEA measured by the potential static method under a symmetric Li//UVEA//Li cell configuration at 22 °C. Note that to accurately measure the transference number, the cell was first activated at 0.2 mA cm^{-2} and 0.2 mAh cm^{-2} to enable the SEI formation and achieve a stable interfacial resistance. Thus, the inserted EIS plots in d showed similar interfacial resistance before and after polarization.

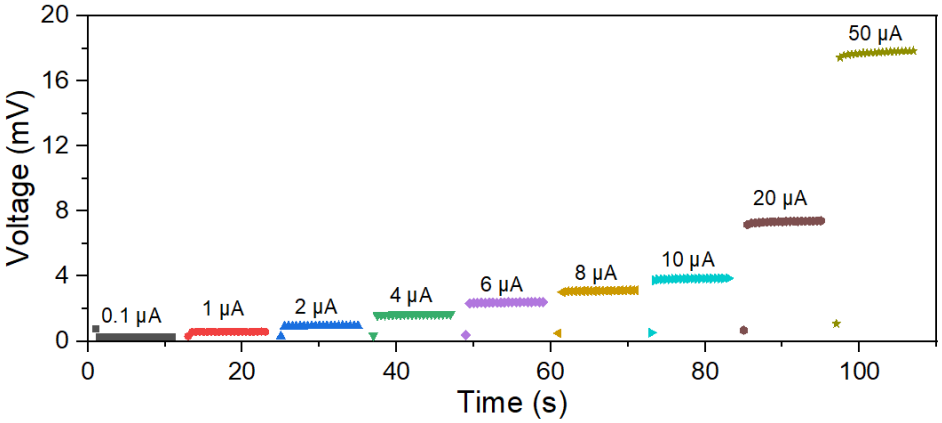

Figure S6. Voltage response of Li//UVEA//Li cells at different applied currents.

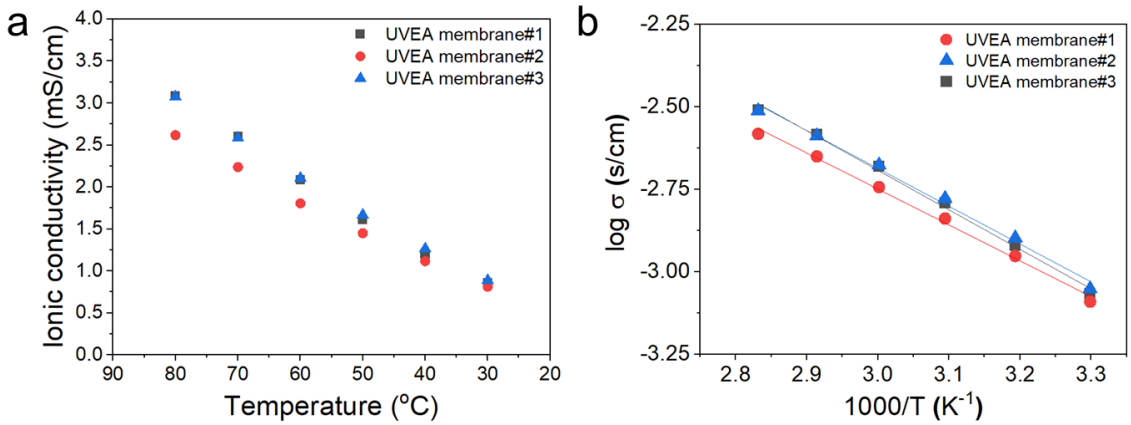

Figure SS7. (a) Ionic conductivity of UVEA membranes at different temperatures measured by the EIS method using a symmetric SS//UVEA//SS cell configuration (SS represents stainless steel). (b) Temperature-dependent ionic conductivity curve of UVEA films showing that the UVEA film exhibits an Arrhenius-type ion conduction mechanism. Note that the melting point of pure SN around 58 °C is not seen here, which is probably due to the amorphization of polymer backbone and SN.

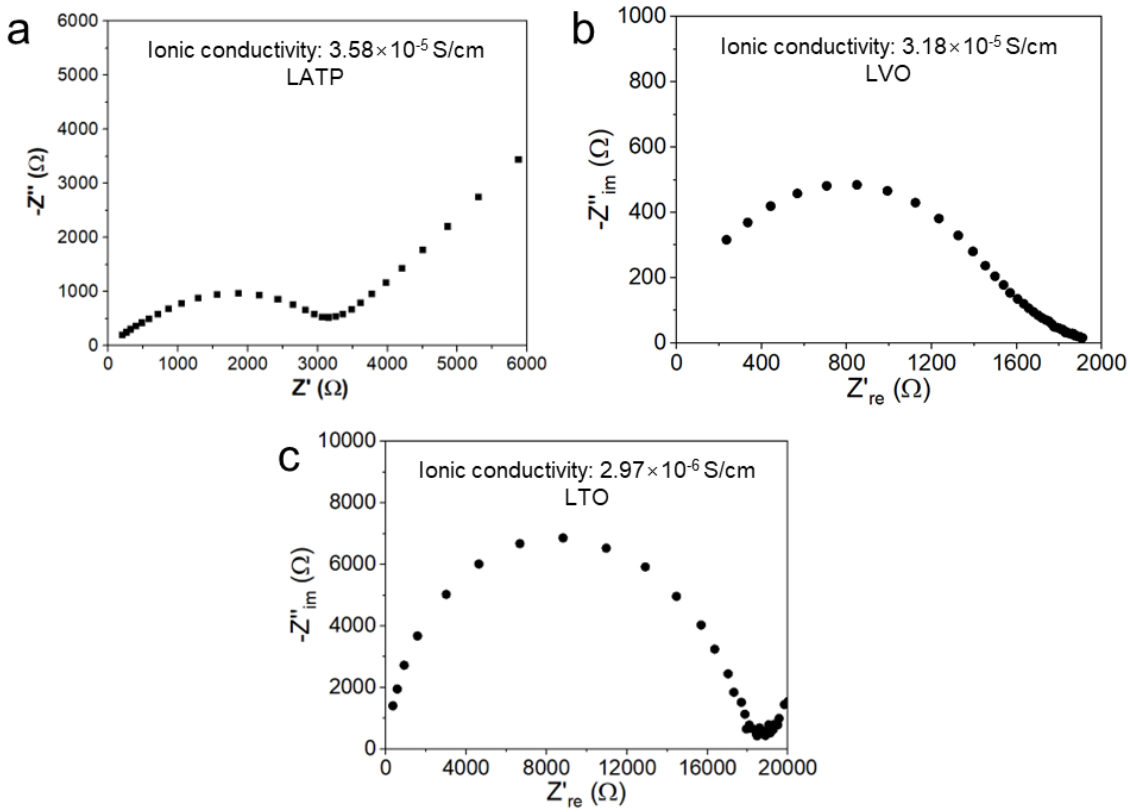

Figure S8. EIS curves of (a) SS//LATP//SS cell, (b) SS//LVO//SS cell, (b) SS//LTO//SS cell, and (c) SS//LTO//SS cell during the ionic conductivity test. SS represents stainless steel. The thickness of LATP, LVP, and LTO pellets is 1360 μm, 675 μm, and 728 μm, respectively. While the surface area of all ceramic pellets is 1.33 cm^2. Noted that the inorganic ceramics for ionic conductivity test is typically thicker than those used for real batteries.

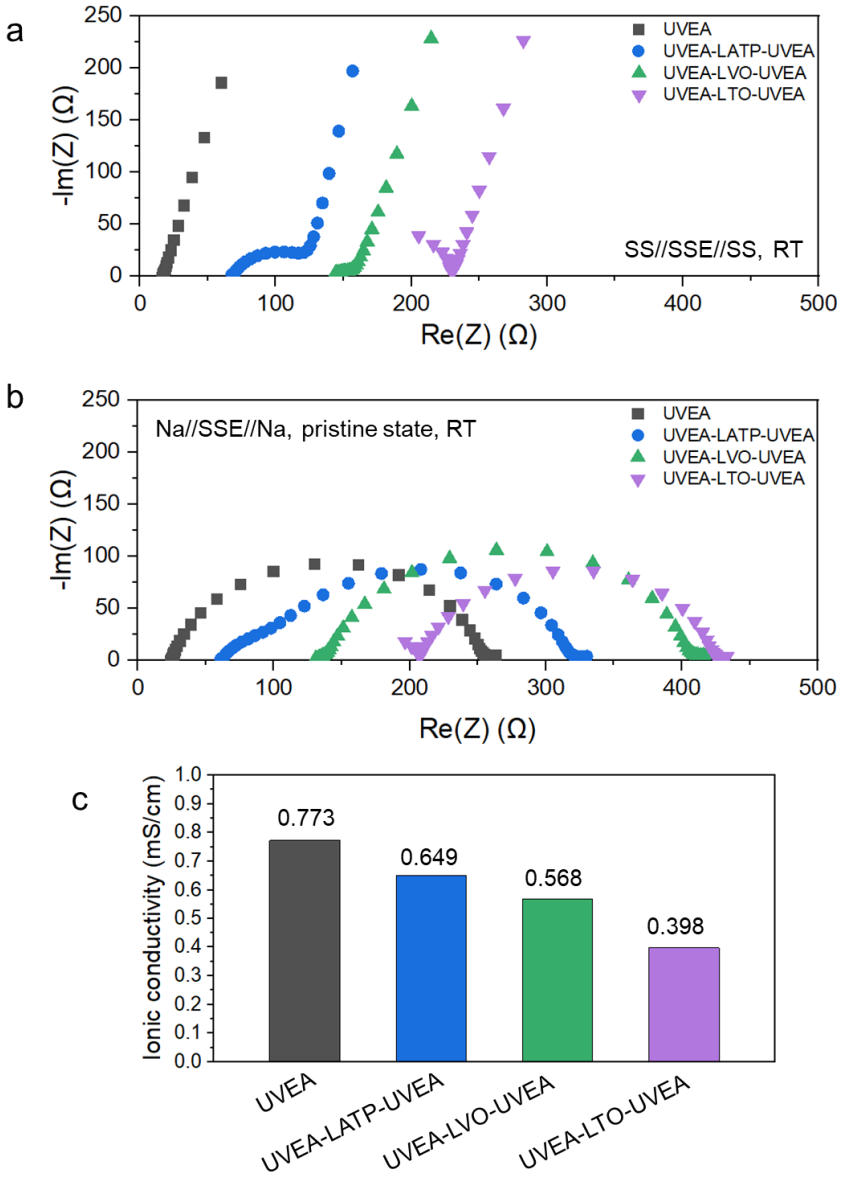

Figure S9. EIS profiles showing the interfacial resistance of symmetric SS//SS cells (a) and Li//Li cells (b) using bare UVEA film and sandwich SSEs at room temperature. SS represents stainless steel. (c) Summary of ionic conductivity of bare UVEA and sandwich SSEs.

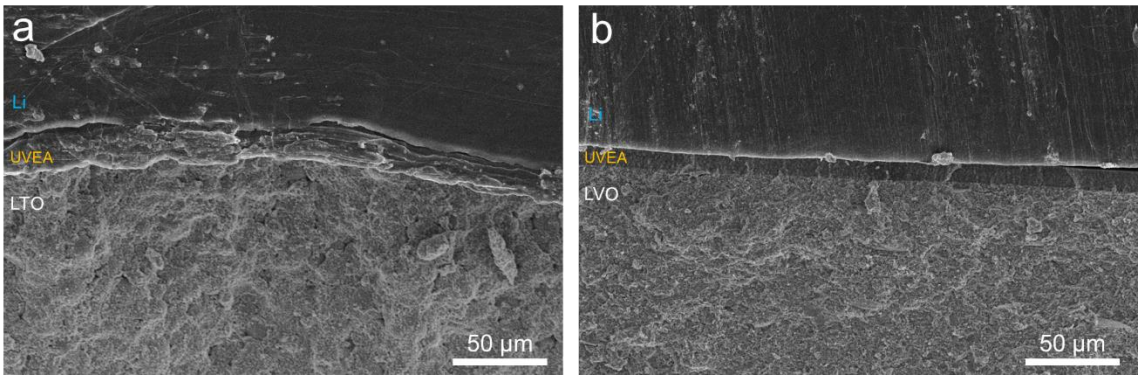

Figure S10. Cross-sectional SEM image showing the good interface contact between UVEA with Li metal, and UVEA with ceramics: (a) LTO; (b) LVO.

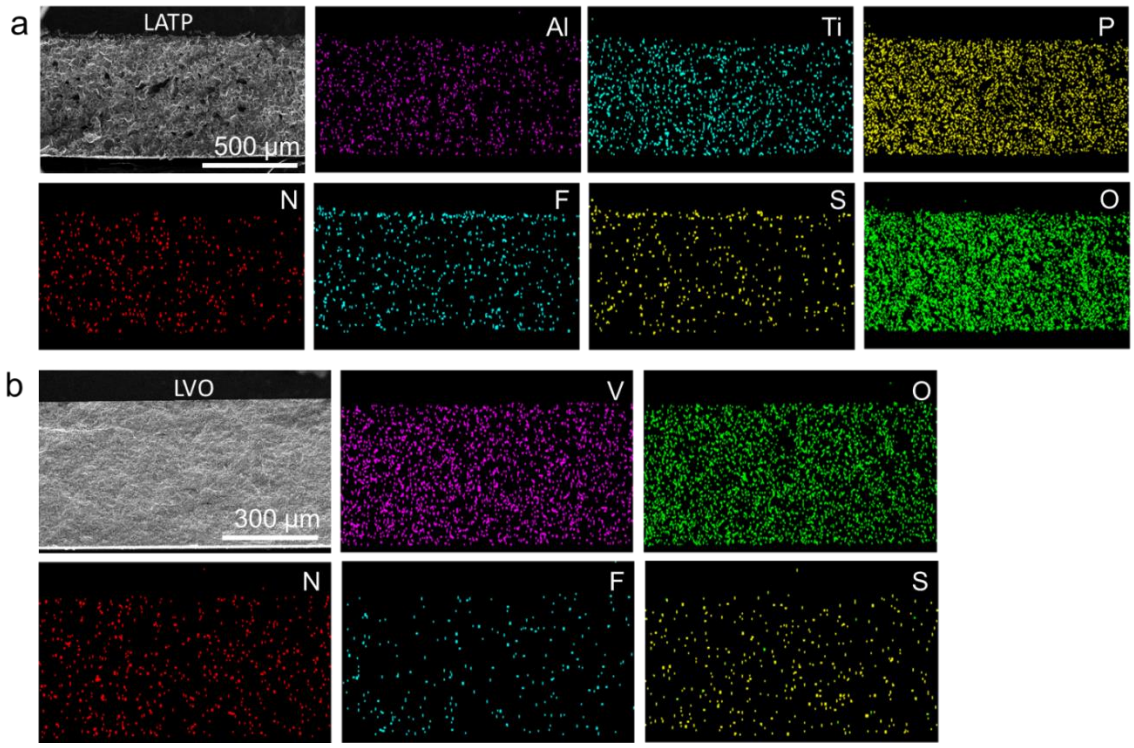

Figure S11. SEM-EDS mapping of (a) LATP and (b) LVO pellets after cycling in Li//UVEA-LATP-UVEA//NMC811 and Li//UVEA//NMC811 cells at 0.2 C for 20 cycles, respectively. The significant N, F, and S signal was attributed to the UVEA penetration into the LAPT and LVO pellets.

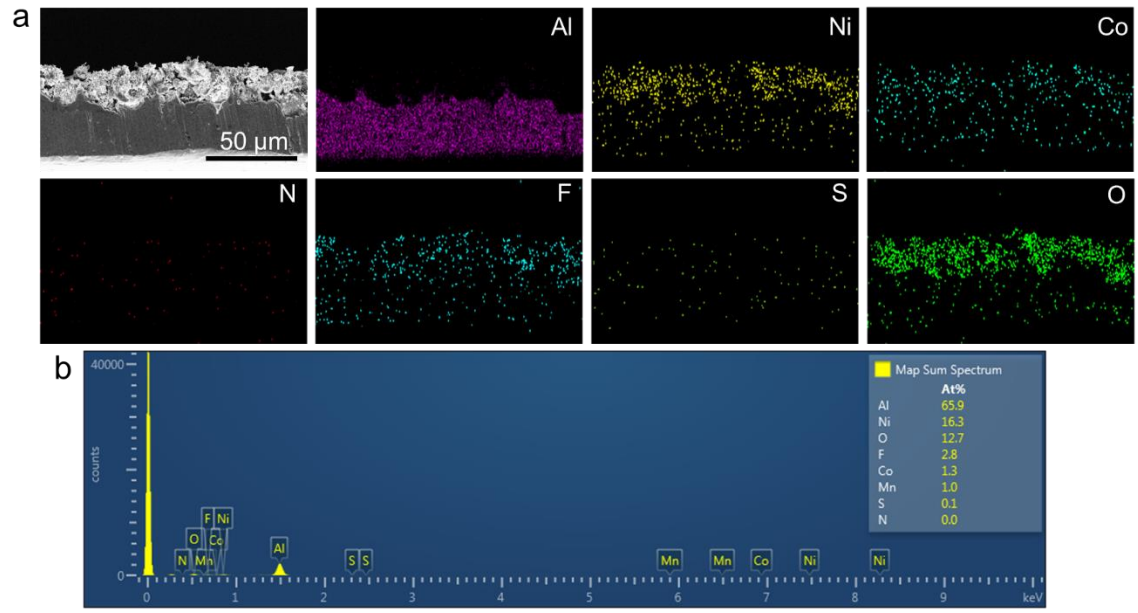

Figure S12. (a) SEM-EDS mapping and (b) corresponding element ratio of pristine NMC811 electrode.

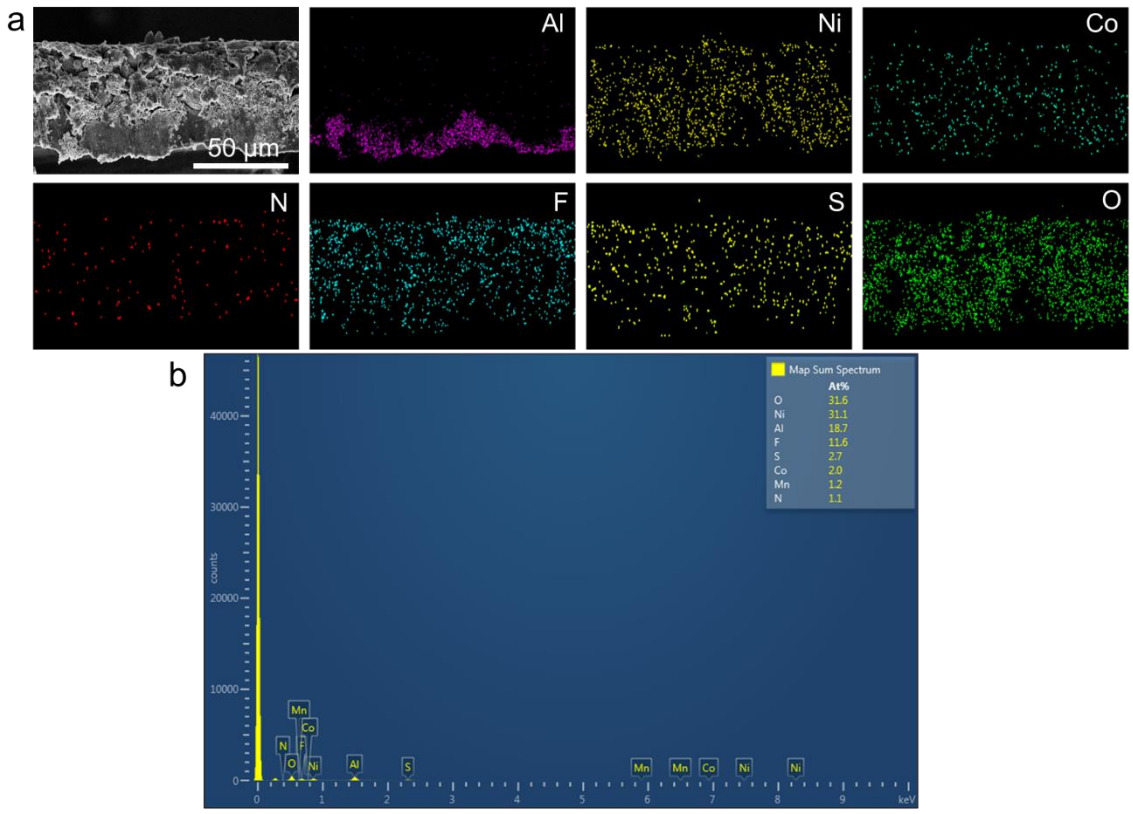

Figure S13. (a) SEM-EDS mapping and (b) corresponding element ratio of cycled NMC811 electrode from Li//UVEA-LATP-UVEA//NMC811. The full cell was cycled at 0.2C for 20 cycles. Compared with negligible N signal in pristine NMC811 electrode (Figure S12), the identified N signal in cycled NMC811 was attributed to the UVEA penetration into the NMC811 cathode, which was consistent with the result in Figure S11.

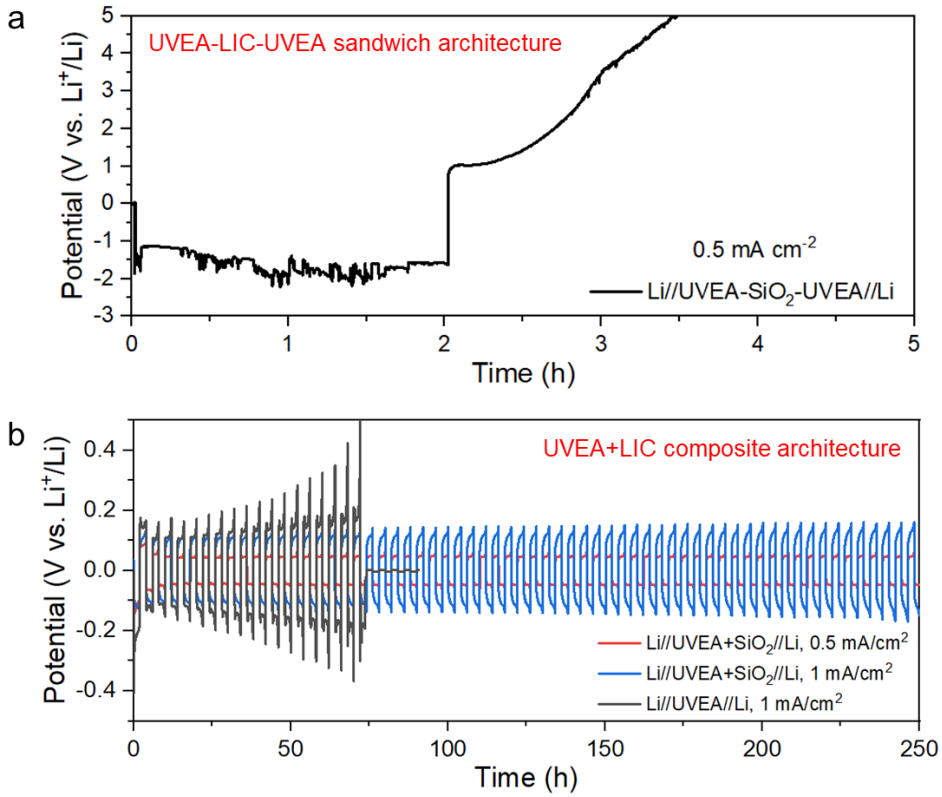

Figure S14. (a) Charge and discharge profiles of symmetric Li//Li cells using sandwich-type UVEA-SiO_2-UVEA as the SSE. The test current density was 0.5 mA cm^{-2}. (b) Charge and discharge profiles of symmetric Li//Li cells using composite-type UVEA+SiO_2 as the SSE, benchmarked with bare UVEA baseline. The plating/stripping time was fixed at 1 h for all cells.

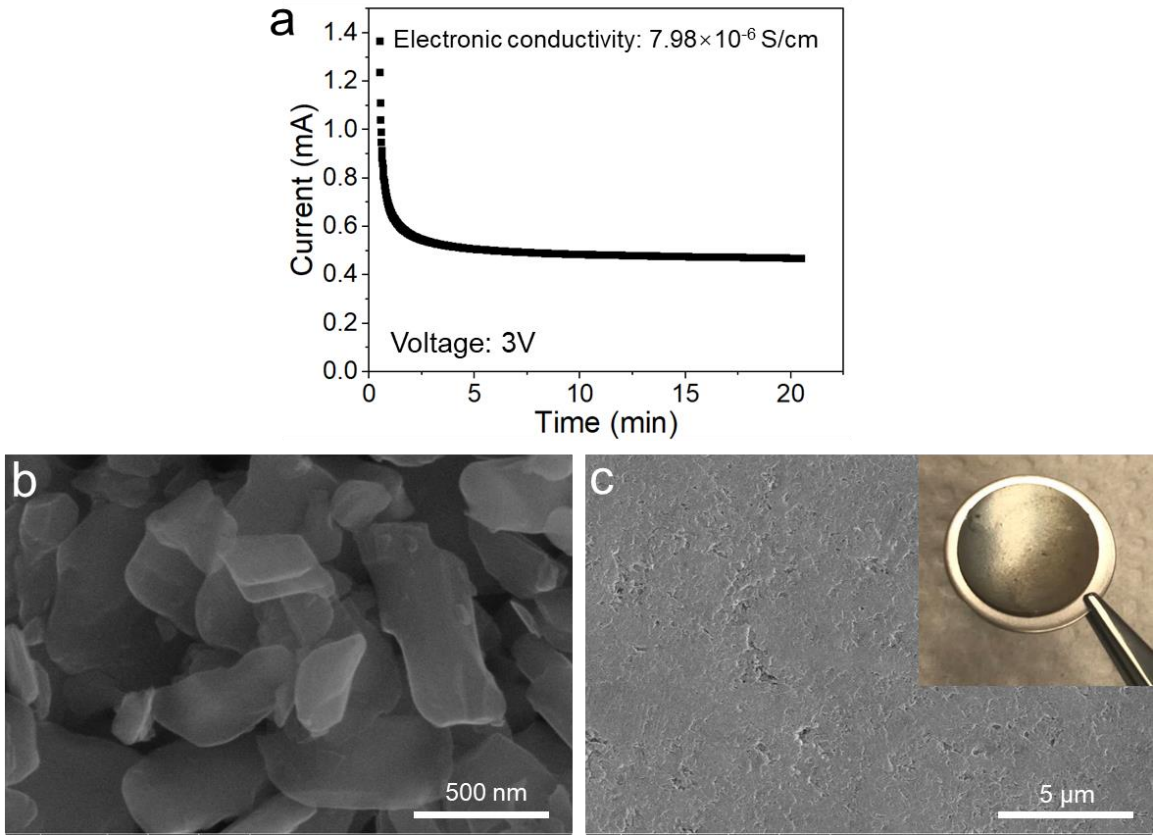

Figure S15. (a) Electronic conductivity test of pristine LVO pellet with a thickness of 675 μm. The applied voltage during the test was controlled at 3 V. SEM images of pristine LVO powder (b) and LVO pellet after cold pressing (c). The inset in d shows the digital image of as-fabricated LVO pellet.

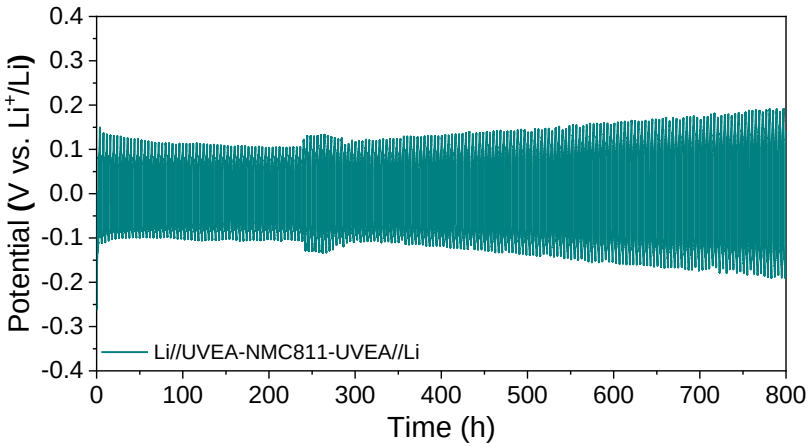

Figure S16. Charge and discharge profiles of symmetric Li//Li cells using sandwich-type UVEA-NMC811-UVEA as the SSE. The plating/stripping current density was 0.5 mA cm^{-2}, and the plating/stripping time was fixed at 1 h.

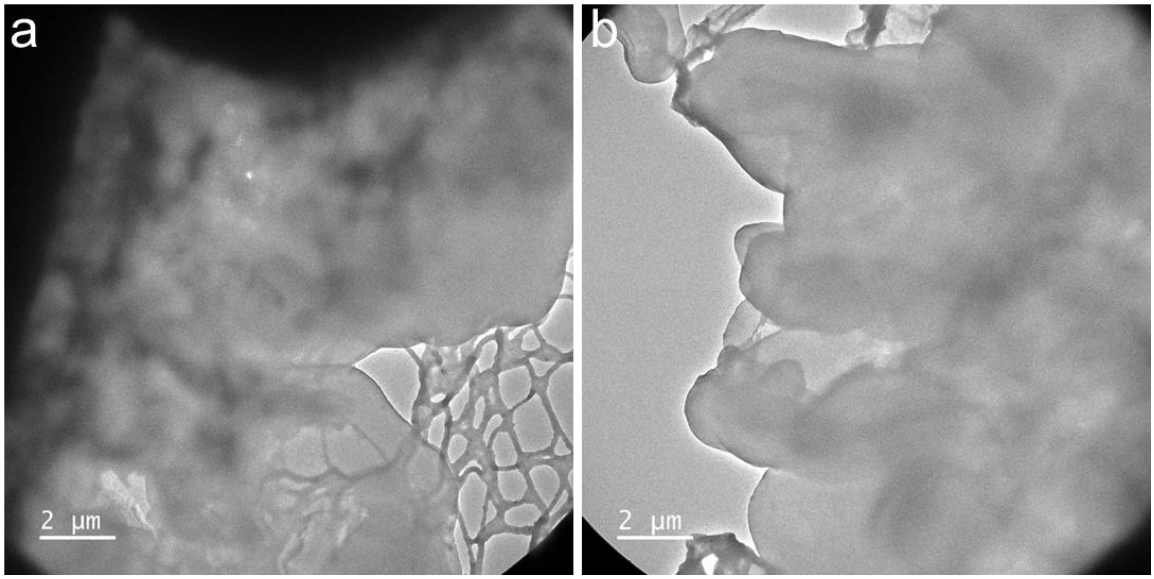

Figure S17. (a, b) Cryo-TEM images showing the morphology of the deposited Li^0 on Cu grid using the UVEA-LATP-UVEA sandwich electrolyte, which were collected from two different sites.

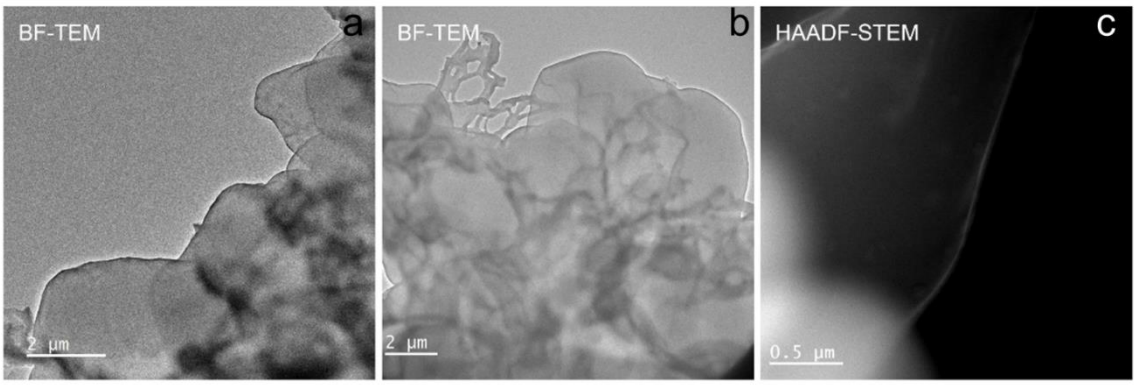

Figure S18. Higher-magnification BF-TEM and HAADF-STEM images of the Li deposits plated by the UVEA-LATP-UVEA sandwich electrolyte. The surface SEI (darker contrast in the BF-TEM modd V.S. brighter contrast in HAADF-STEM mode) are clearly visible in these images.

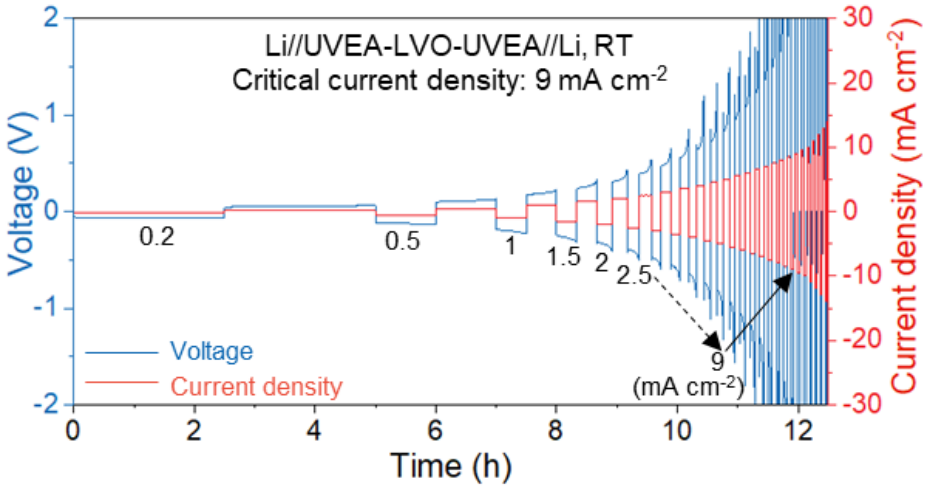

Figure S19. Critical current density of UVEA-LVO-UVEA tested in symmetric Li//Li cells at 22 ^{o}C (RT). The Li//Li symmetric cell was cycled under step-up current densities with a constant plating/stripping capacity of 0.5 mAh cm^{-2}, and no short circuit occurred before 9 mA cm^{-2}.

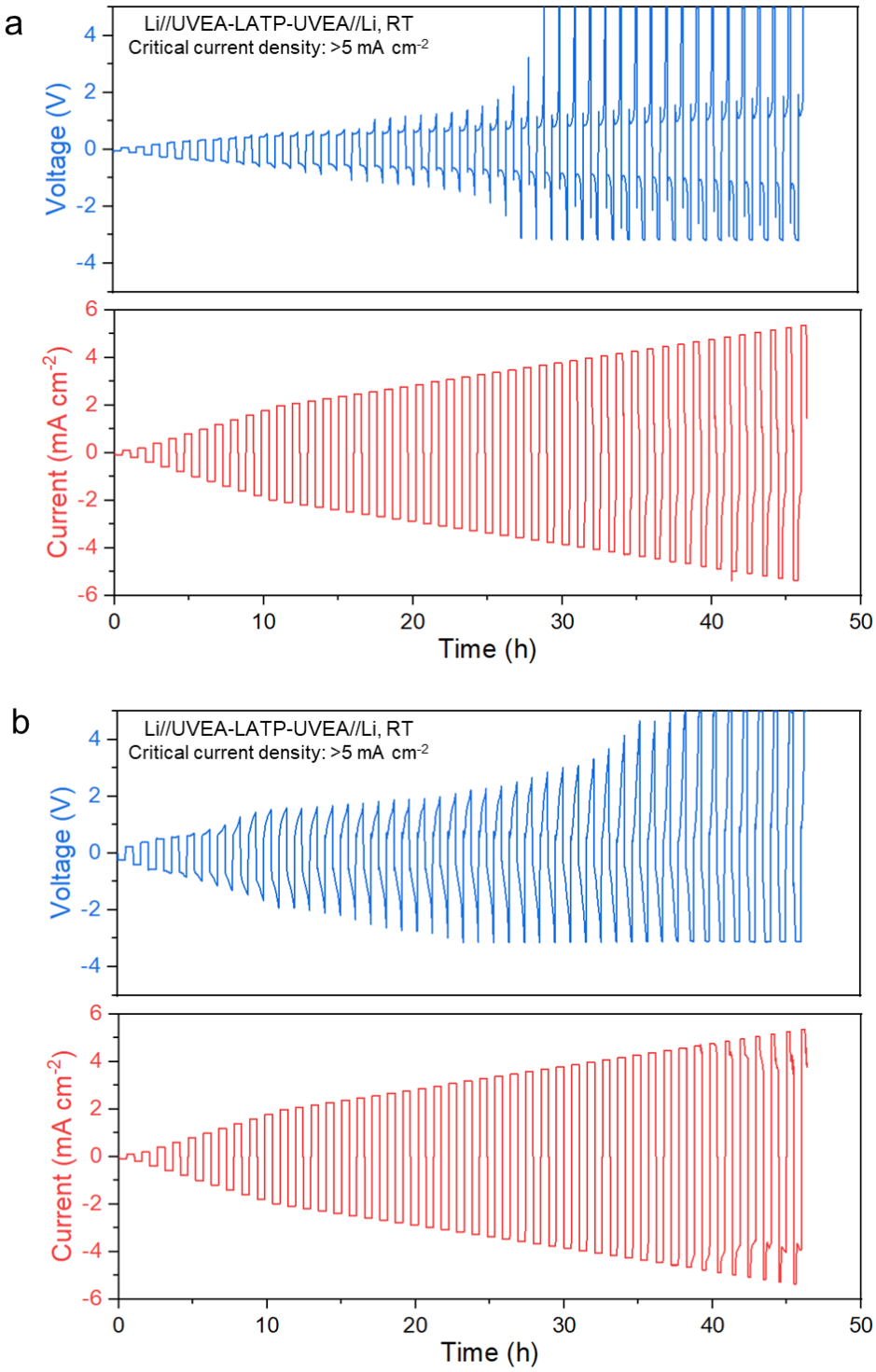

Figure S20. Critical current density of UVEA-LATP-UVEA (a) and UVEA-LTO-UVEA tested in symmetric Li//Li cells at 22 ^{o}C (RT). The Li//Li symmetric cell was cycled under step-up current densities with a constant plating/stripping time of 0.5 h, and no short circuit occurred before 5 mA cm^{-2}.

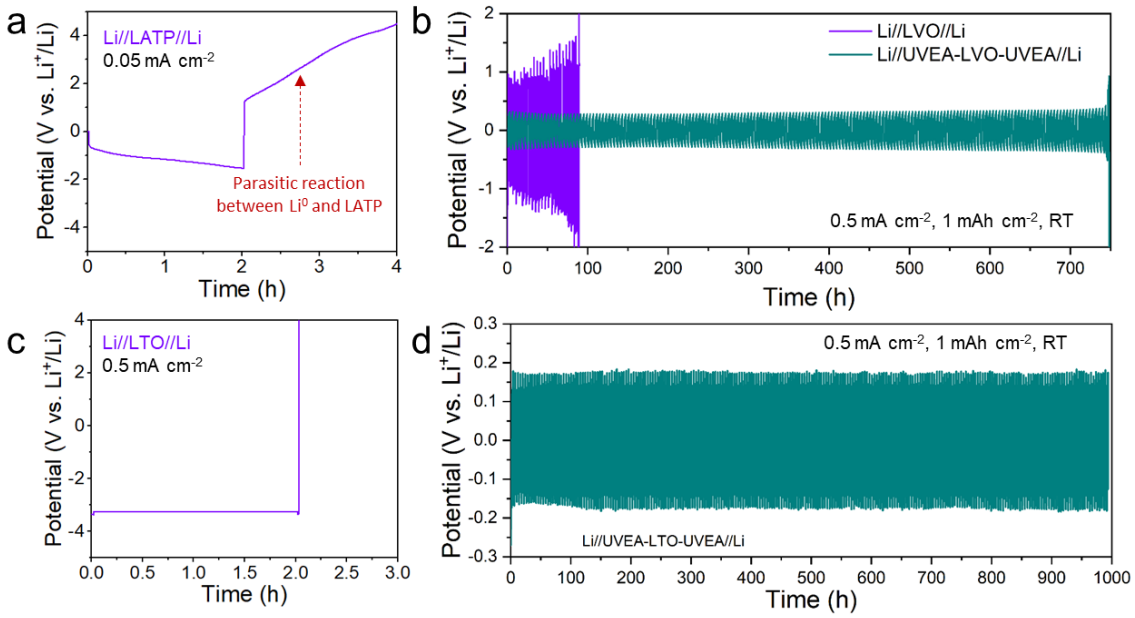

Figure S21. (a) Discharge/charge profile of solid-state Li//LATP//Li battery at a current density of 0.05 mA cm^{-2} showing that the symmetric cell using bare LATP baseline can be hardly initiated. (b-f) Discharge/charge profile of solid-state battery at a current density of 0.5 mA cm^{-2} and a cycling capacity of 1 mAh cm^{-2}: (b) Li//LVO//Li and Li//UVEA-LVO-UVEA//Li; (c) Li//LTO//Li; (d) Li//UVEA-LTO-UVEA//Li.

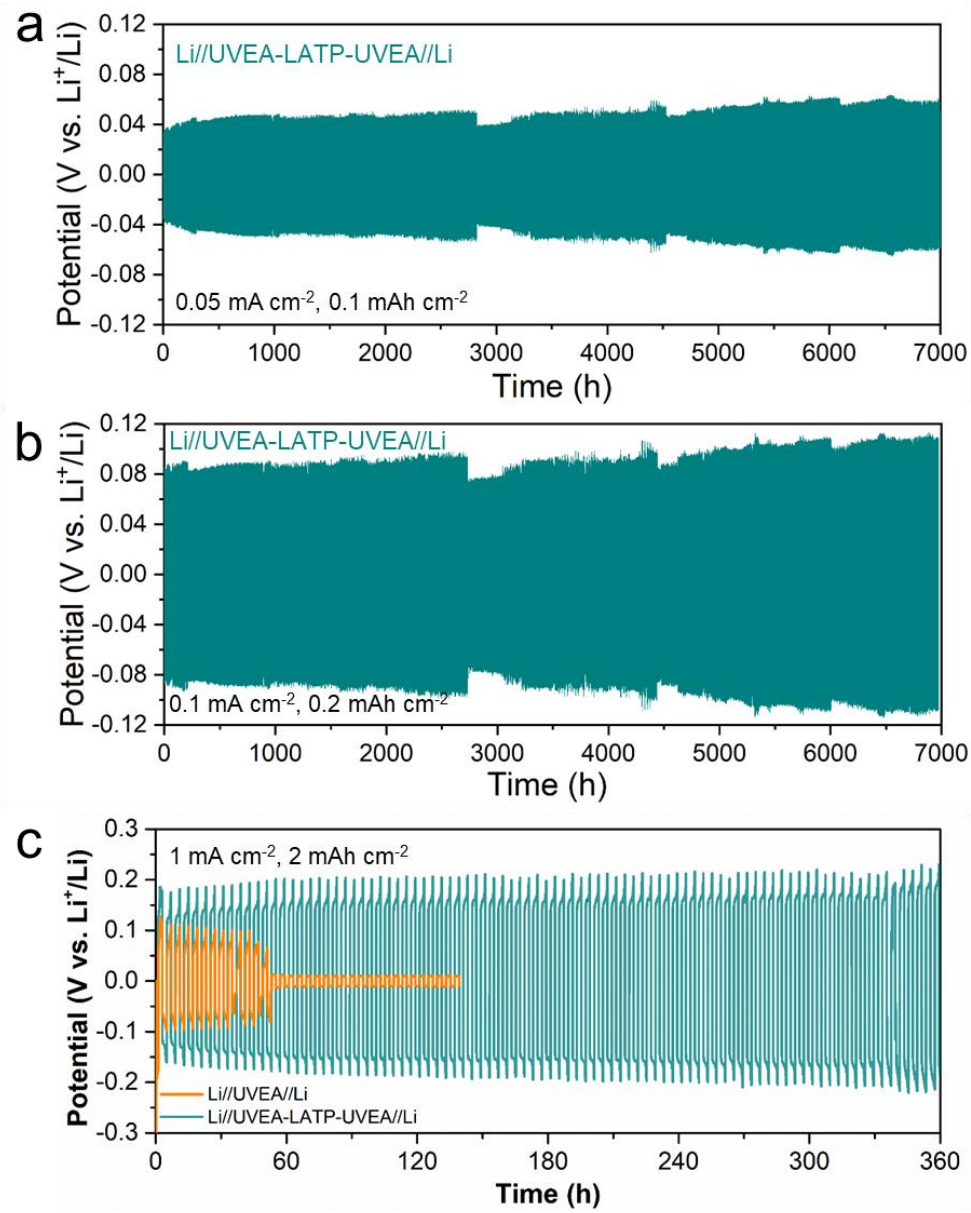

Figure S22. Discharge/charge profile of solid-state Li//UVEA-LATP-UVEA//Li battery at varied current densities and cycling capacity: (a) 0.05 mA cm^{-2}, 0.1 mAh cm^{-2}; (b) 0.1 mA cm^{-2}, 0.2 mAh cm^{-2}; (c) 0.5 mA cm^{-2}, 1 mAh cm^{-2}.

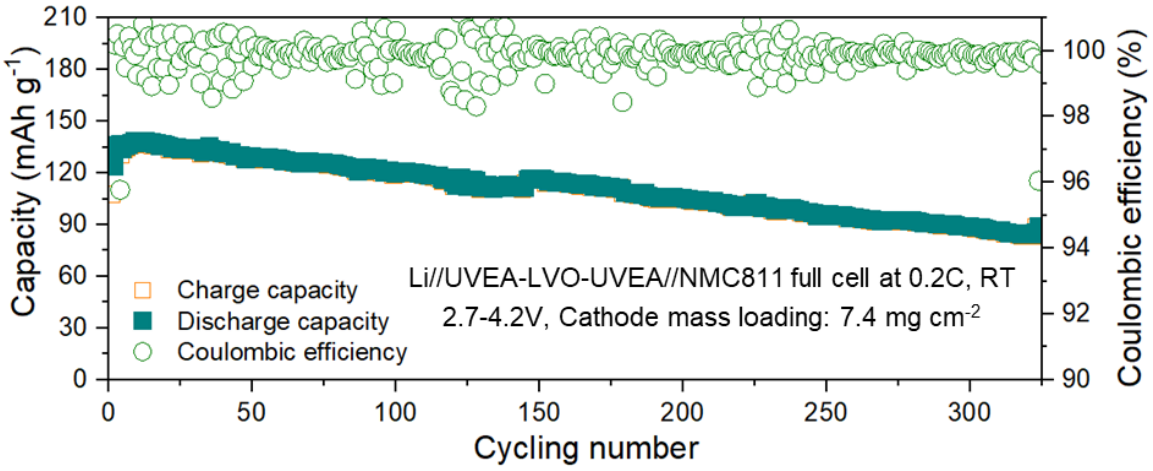

Figure S23. Cycling stability of Li//UVEA-LVO-UVEA//NMC811 cells at 0.2 C with the test voltage window of 2.7-4.2V. The areal mass loading of NMC811 is ~7.4 mg cm^{-2}.

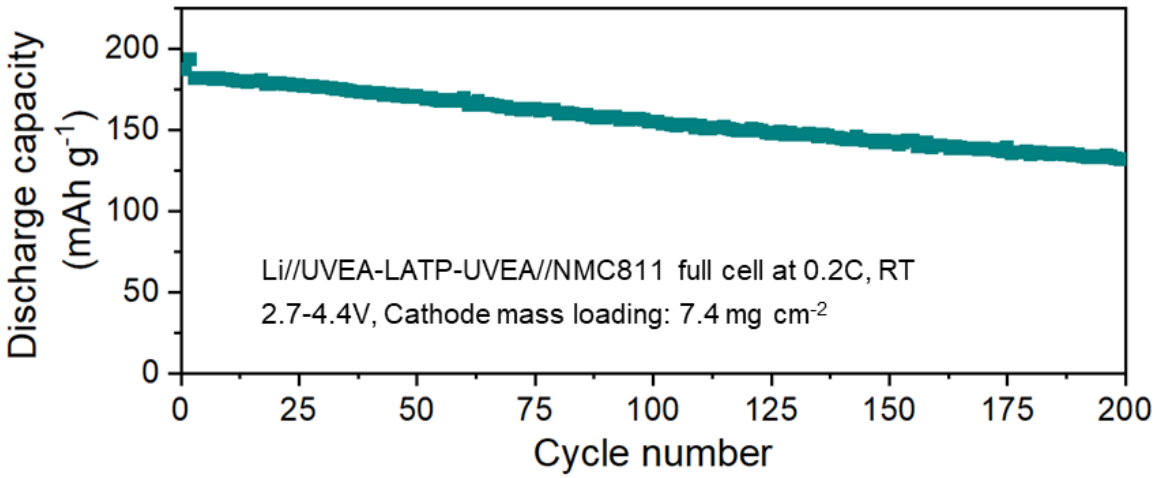

Figure S24. Cycling stability of Li//UVEA-LATP-UVEA//NMC811 cells at 0.2 C with a test voltage window of 2.7-4.4V. The areal mass loading of NMC811 is ~7.4 mg cm^{-2}.

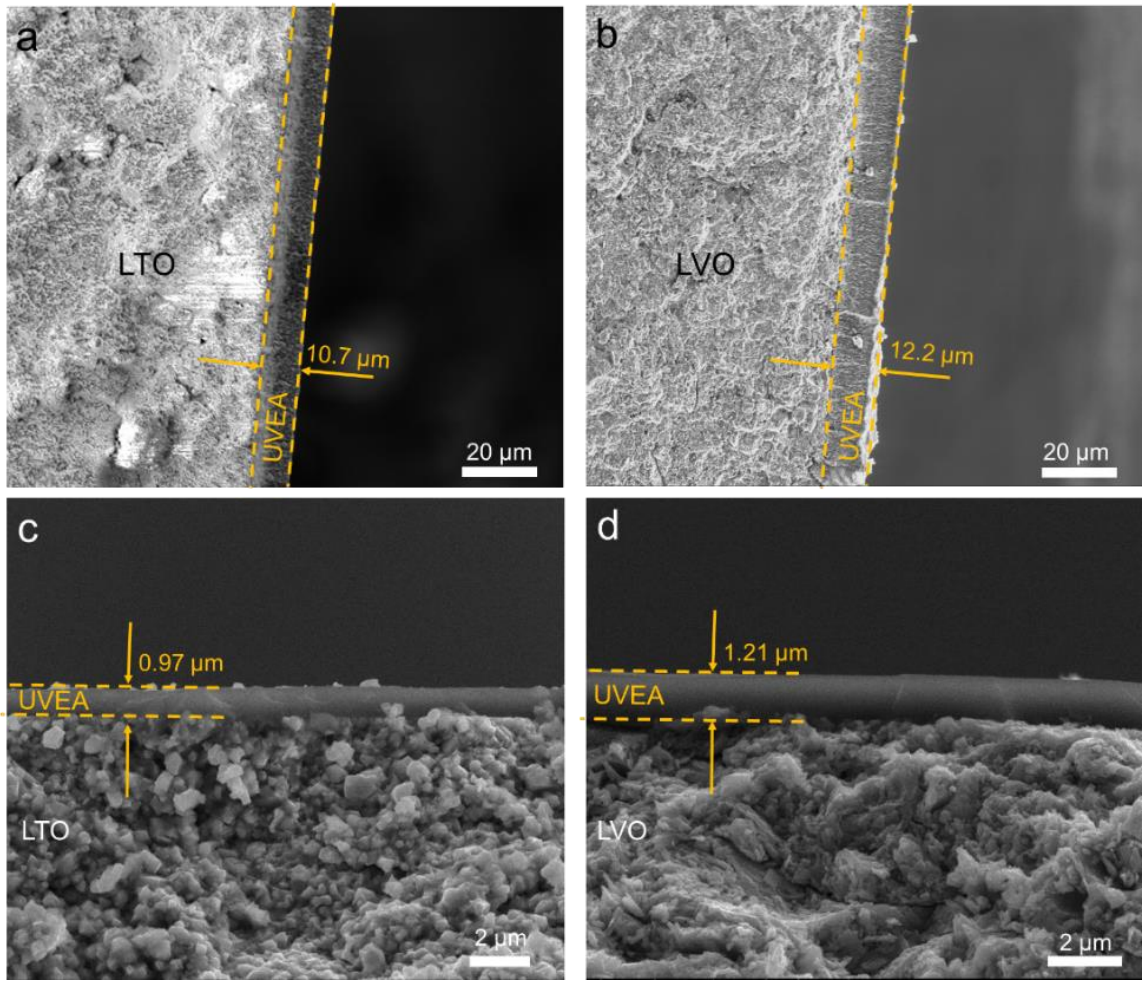

Figure S25. (a, b) SEM images of thin UVEA layer on (a) LTO pellet and (b) LVO pellet using the dip-coating method. (c, d) SEM images of thin UVEA layer on (c) LTO pellet and (d) LVO pellet using the spin-coating method. The spinning speed was 2000 r/min and the spinning time was 30s.

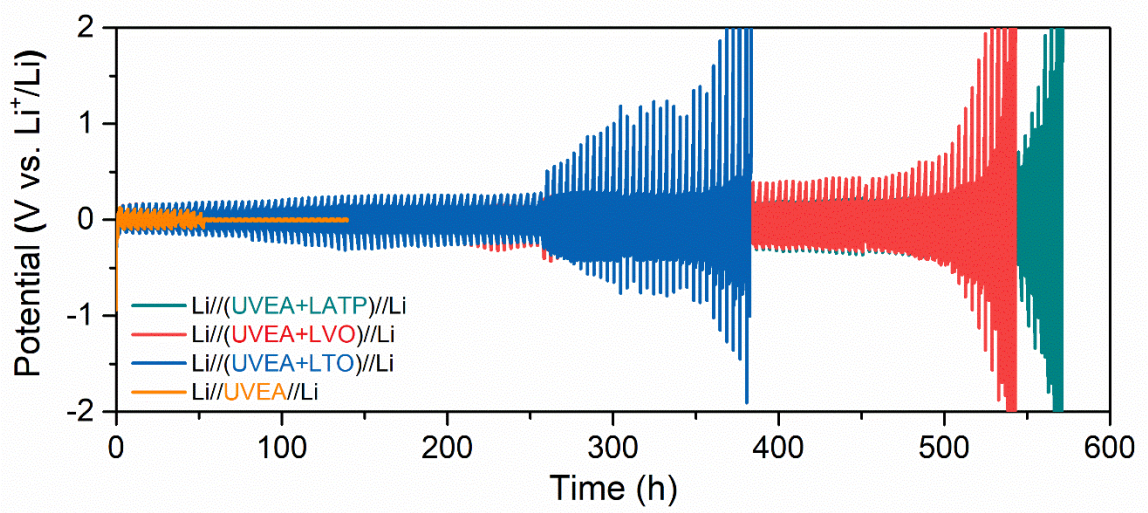

Figure S26. Discharge/charge profiles of solid-state Li//Li symmetric cells based on different composite SSEs. The cycling current density was 1 mA cm^{-2} and the cycling capacity was 2 mAh cm^{-2}.

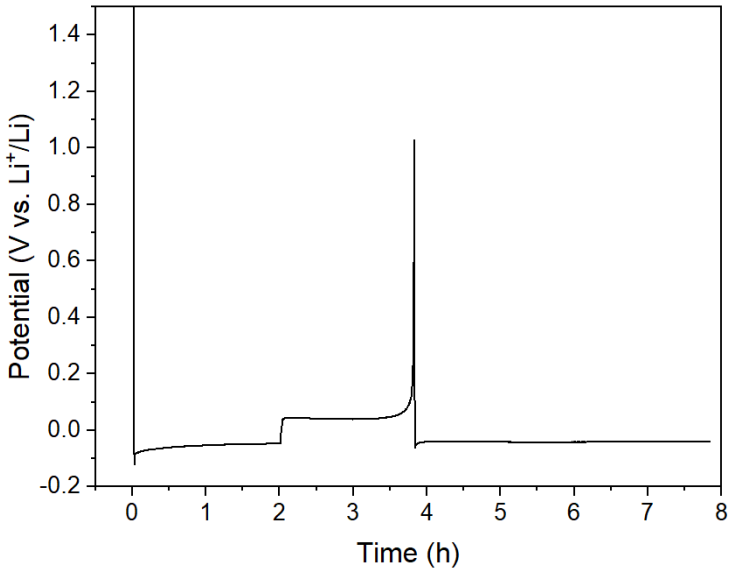

Figure S27. Typical voltage-time profile of Li//Cu cell for depositing 2 mAh cm^{-2} of Li metal on Cu foil. The current density during the first-cycle activation and the subsequent Li plating was 0.5 mA cm^{-2}.

Table S1. Summary of applied currents, response voltage, and calculated DCR value of UVEA film in the Li//UVEA//Li cell.

Applied current (μA)		**Response Voltage (mV)**		**DCR (×1000 ohm)**	
I_1	0.1	V_1	0.278		/
I_2	1	V_2	0.587	$I_1 \rightarrow I_2$	0.343
I_3	2	V_3	0.942	$I_2 \rightarrow I_3$	0.355
I_4	4	V_4	1.656	$I_3 \rightarrow I_4$	0.357
I_5	6	V_5	2.393	$I_4 \rightarrow I_5$	0.369
I_6	8	V_6	3.106	$I_5 \rightarrow I_6$	0.357
I_7	10	V_7	3.849	$I_6 \rightarrow I_7$	0.372
I_8	20	V_8	7.371	$I_7 \rightarrow I_8$	0.352
I_9	50	V_9	17.756	$I_8 \rightarrow I_9$	0.346

Table S2. Summary of ionic and electronic conductivities of different LICs and sandwich SSEs used in this work.

Electrolyte	**Ionic conductivity (S/cm, room temperature)**	**Electronic conductivity (S/cm, room temperature)**
UVEA	7.73×10^{-4}	6.65×10^{-9}
LATP	3.58×10^{-5}	8.07×10^{-7}
LVO	3.18×10^{-5}	7.54×10^{-6}
LTO	2.97×10^{-5}	1.27×10^{-8}
UVEA-LATP-UVEA	6.49×10^{-4}	/
UVEA-LVO-UVEA	5.68×10^{-4}	/
UVEA-LTO-UVEA	3.98×10^{-4}	/

Table S3. Comparison of electrochemical performance of sandwich SSE (this work) with recently reported LIC-based SSE.

Solid state electrolyte	Electrochemical stability window (V vs. Li^+/Li)	Critical current density (mA cm^{-2})	Lithium anode lifetime (hours)	Cumulative capacity (mAh cm^{-2})	Full cell performance (Capacity retention)	Reference
UVEA-LATP-UVEA (multi-layer)	0-4.6	>14 (@0.5 mAh cm^{-2})	2500@0.5 mA cm^{-2}	1250	87% after 350 cycles, 0.2C at RT (NMC811, loading: 7.4 mg cm^{-2})	This work
			7000@0.1 mA cm^{-2}	700		
Plastic-crystal-embedded elastomer electrolyte (PCEE) (composite)	0-4.6	N.A.	1500@10 mA cm^{-2}	15000	88% after 100 cycles, at 30 °C (NMC83, loading: >10 mg cm^{-2})	6
ZnO-coated LATP (multi-layer)	N.A.	N.A.	1000@0.2 mA cm^{-2}	200	88% after 100 cycles, 0.1C at RT (LFP, loading: 2.55 mg cm^{-2})	7
BN-coated LATP (multi-layer)	0-4.5	N.A.	500@0.3 mA cm^{-2}	150	96% after 500 cycles, 0.5C at 60 °C (LFP, loading: 2.4 mg cm^{-2})	8
LPSCl–LGPS–LPSCl (multi-layer)	N.A.	N.A.	1800@0.25 mA cm^{-2}	450	81.3% after 2000 cycles, 1.5C at 55 °C (NMC811, loading: 2 mg cm^{-2})	9
PEO-LATP (composite)	N.A.	N.A.	1800@1 mA cm^{-2} (at 60 °C)	1800	70% after 1000 cycles, 0.5C at 60 °C (LFP, loading: 5 mg cm^{-2})	10
$LiAlO_2$-coated LLCZN (multi-layer)	N.A.	0.75	N.A.	N.A.	N.A.	11
h-BN-coated LLZTO (multi-layer)	N.A.	0.9	200@0.5 mA cm^{-2} (at 60 °C)	100	91.5% after 100 cycles, 0.2C at 60 °C (LFP, loading: 8.8 mg cm^{-2})	12
Li-LLZO	N.A.	13.3 (@0.36 mAh cm^{-2})	80@2.2 mA cm^{-2}	176	N.A.	13
COF-coated LLZTO (multi-layer)	N.A.	3	55@0.1 mA cm^{-2}	5.5	89% after 360 cycles, 0.5C at RT (LFP, loading: 2~3 mg cm^{-2})	14
3D LLZO	N.A.	10 (@7.5 mAh cm^{-2})	N.A.	N.A.	N.A.	15
LiF-LPS (multi-layer)	N.A.	>2	350@0.3 mA cm^{-2}	105	>90% after 50 cycles, 0.3 mA cm^{-2} (LCO, loading: 1 mAh cm^{-2})	16
PEO-LLZTO (composite)	0-4.75	>3 (@3 mAh cm^{-2})	700@3 mA cm^{-2}	2100	>90% after 200 cycles, 0.1C (LFP, loading: 1.46 mAh cm^{-2})	17
PEO-PPO-SiO2 (composite)	0-6.5	>4.8 (@1.2 mAh cm^{-2})	2010@1.2 mA cm^{-2} 1710@2.4 mA cm^{-2}	4104 (at 2.4 mA cm^{-2})	~100% after 100 cycles, 0.5C (LFP, loading: 1.5~1.9 mg cm^{-2})	18

References

1. Zhang, Q.; Brady, A. B.; Pelliccione, C. J.; Bock, D. C.; Bruck, A. M.; Li, J.; Sarbada, V.; Hull, R.; Stach, E. A.; Takeuchi, K. J.; Takeuchi, E. S.; Liu, P.; Marschilok, A. C., Investigation of Structural Evolution of Li1.1V3O8 by In Situ X-ray Diffraction and Density Functional Theory Calculations. *Chem. Mater.* **2017,** *29* (5), 2364-2373.
2. Zhang, Q.; Bruck, A. M.; Bock, D. C.; Li, J.; Sarbada, V.; Hull, R.; Stach, E. A.; Takeuchi, K. J.; Takeuchi, E. S.; Marschilok, A. C., Visualization of structural evolution and phase distribution of a lithium vanadium oxide (Li1.1V3O8) electrode via an operando and in situ energy dispersive X-ray diffraction technique. *Phys. Chem. Chem. Phys.* **2017,** *19* (21), 14160-14169.
3. He, Y.; Zou, P.; Bak, S.-M.; Wang, C.; Zhang, R.; Yao, L.; Du, Y.; Hu, E.; Lin, R.; Xin, H. L., Dual Passivation of Cathode and Anode through Electrode–Electrolyte Interface Engineering Enables Long-Lifespan Li Metal–SPAN Batteries. *ACS Energy Letters* **2022,** *7* (9), 2866-2875.
4. Zhang, Q.; Liu, K.; Ding, F.; Li, W.; Liu, X.; Zhang, J., Safety-Reinforced Succinonitrile-Based Electrolyte with Interfacial Stability for High-Performance Lithium Batteries. *ACS Applied Materials & Interfaces* **2017,** *9* (35), 29820-29828.
5. He, R.; Echeverri, M.; Ward, D.; Zhu, Y.; Kyu, T., Highly conductive solvent-free polymer electrolyte membrane for lithium-ion batteries: Effect of prepolymer molecular weight. *J. Membr. Sci.* **2016,** *498*, 208-217.
6. Lee, M. J.; Han, J.; Lee, K.; Lee, Y. J.; Kim, B. G.; Jung, K. N.; Kim, B. J.; Lee, S. W., Elastomeric electrolytes for high-energy solid-state lithium batteries. *Nature* **2022,** *601* (7892), 217-222.
7. Hao, X.; Zhao, Q.; Su, S.; Zhang, S.; Ma, J.; Shen, L.; Yu, Q.; Zhao, L.; Liu, Y.; Kang, F.; He, Y. B., Constructing Multifunctional Interphase between Li1.4Al0.4Ti1.6(PO4)3 and Li Metal by Magnetron Sputtering for Highly Stable Solid‐State Lithium Metal Batteries. *Advanced Energy Materials* **2019,** *9* (34).
8. Cheng, Q.; Li, A.; Li, N.; Li, S.; Zangiabadi, A.; Li, T.-D.; Huang, W.; Li, A. C.; Jin, T.; Song, Q.; Xu, W.; Ni, N.; Zhai, H.; Dontigny, M.; Zaghib, K.; Chuan, X.; Su, D.; Yan, K.; Yang, Y., Stabilizing Solid Electrolyte-Anode Interface in Li-Metal Batteries by Boron Nitride-Based Nanocomposite Coating. *Joule* **2019,** *3* (6), 1510-1522.
9. Ye, L.; Li, X., A dynamic stability design strategy for lithium metal solid state batteries. *Nature* **2021,** *593* (7858), 218-222.
10. Yu, X.; Manthiram, A., A Long Cycle Life, All-Solid-State Lithium Battery with a Ceramic–Polymer Composite Electrolyte. *ACS Applied Energy Materials* **2020,** *3* (3), 2916-2924.
11. Song, Y.; Yang, L.; Zhao, W.; Wang, Z.; Zhao, Y.; Wang, Z.; Zhao, Q.; Liu, H.; Pan, F., Revealing the Short‐Circuiting Mechanism of Garnet‐Based Solid‐State Electrolyte. *Advanced Energy Materials* **2019,** *9* (21), 1900671.
12. Rajendran, S.; Pilli, A.; Omolere, O.; Kelber, J.; Arava, L. M. R., An All-Solid-State Battery with a Tailored Electrode–Electrolyte Interface Using Surface Chemistry and Interlayer-Based Approaches. *Chem. Mater.* **2021,** *33* (9), 3401-3412.
13. Zheng, H.; Wu, S.; Tian, R.; Xu, Z.; Zhu, H.; Duan, H.; Liu, H., Intrinsic lithiophilicity of Li‐garnet electrolytes enabling high‐rate lithium cycling. *Adv. Funct. Mater.* **2020,** *30* (6), 1906189.

14. Cheng, Z.; Xie, M.; Mao, Y.; Ou, J.; Zhang, S.; Zhao, Z.; Li, J.; Fu, F.; Wu, J.; Shen, Y., Building Lithiophilic Ion‐Conduction Highways on Garnet‐Type Solid‐State Li+ Conductors. *Advanced Energy Materials* **2020,** *10* (24), 1904230.
15. Hitz, G. T.; McOwen, D. W.; Zhang, L.; Ma, Z.; Fu, Z.; Wen, Y.; Gong, Y.; Dai, J.; Hamann, T. R.; Hu, L.; Wachsman, E. D., High-rate lithium cycling in a scalable trilayer Li-garnet-electrolyte architecture. *Mater. Today* **2019,** *22*, 50-57.
16. Fan, X.; Ji, X.; Han, F.; Yue, J.; Chen, J.; Chen, L.; Deng, T.; Jiang, J.; Wang, C., Fluorinated solid electrolyte interphase enables highly reversible solid-state Li metal battery. *Science advances* **2018,** *4* (12), eaau9245.
17. Zhang, J.; Zhao, N.; Zhang, M.; Li, Y.; Chu, P. K.; Guo, X.; Di, Z.; Wang, X.; Li, H., Flexible and ion-conducting membrane electrolytes for solid-state lithium batteries: Dispersion of garnet nanoparticles in insulating polyethylene oxide. *Nano Energy* **2016,** *28*, 447-454.
18. Tang, S.; Lan, Q.; Xu, L.; Liang, J.; Lou, P.; Liu, C.; Mai, L.; Cao, Y.-C.; Cheng, S., A novel cross-linked nanocomposite solid-state electrolyte with super flexibility and performance for lithium metal battery. *Nano Energy* **2020,** *71*.